# Seismic imaging of reservoir flow properties: Time-lapse pressure changes

**D. W. Vasco***

## ABSTRACT

Time-lapse fluid pressure and saturation estimates are sensitive to reservoir flow properties such as permeability. In fact, given time-lapse estimates of pressure and saturation changes, one may define a linear partial differential equation for permeability variations within the resevoir. The resulting linear inverse problem can be solve quite efficiently using sparse matrix techniques. An application to a set of crosswell saturation and pressure estimates from a $CO_2$ flood at the Lost Hills field in California demonstrates the utility of this approach. From the crosswell estimates detailed estimates of reservoir permeability are produced. The resulting permeability estimates agree with a permeability log in an adjacent well and are in accordance with water and $CO_2$ saturation changes in the interwell region.

Keywords (Time-lapse geophysics, reservoir characterization, permeability estimation)

*Earth Sciences Division, Berkeley Laboratory, Berkeley, CA 94720

## INTRODUCTION

Three-dimensional reflection seismic imaging has proven particularly successful in defining reservoir structure (Yilmaz 2001). Using three-dimensional reflection data it is now possible to delineate intricate patterns of faulting, providing high quality images of tectonic features (Bahorich and Farmer 1995, Gersztenkorn and Marfurt 1999, Cohen and Coifman 2002). Increasingly, three-dimensional time-lapse surveys are used to monitor changes in the pressure and saturation due to oil and gas production. As such, time-lapse seismic observations serve as a tool for monitoring production (Jack 1997).

The next step is to utilize time-lapse geophysical data for reservoir characterization. That is, to image the flow properties, such a permeability, within the reservoir. At this time, there have only been a handful of attempts to formally characterize a reservoir based upon time-lapse observations (Landa and Horne 1997, Huang et al. 1998, He et al. 1998, Vasco et al. 2003). These investigations have concentrated on time-lapse estimates of saturation changes and their relationship to reservoir permeability variations. One shortcoming associated with the use of saturation changes is that the permeability estimates are for those portions of the reservoir which have undergone changes in fluid content. For example, regions in the reservoir which have been encroached by an advancing water front. In many cases one would like to have estimates of permeability ahead of an advancing water front in order to predict the propagation of the oil and/or water. To accomplish this one must monitor some property of the reservoir which is sensitive to permeability yet changes throughout the reservoir, not just where there are changes in pore fluid content. One such property is reservoir pore pressure. Recently, several studies have outlined procedures for determining reservoir pore pressure changes using time-lapse seismic observations (Tura and Lumley 1998, Brevik 1999, Landro 2001). Thus, there is the possibility of observing pore pressure changes within a producing reservoir.

In this paper I describe a technique which uses time-lapse estimates of pore pressure changes to infer reservoir permeabilities. Thus, the method has the potential to estimate permeabilities throughout the reservoir, not just in areas which have undergone saturation changes. The procedure is relatively simple to derive and implement. Furthermore, the resulting inverse problem for reservoir permeability is linear. As a result, it is possible to estimate reservoir permeability directly and to assess the solution using methods from linear inverse theory. The technique I describe is efficient and robust and I illustrate it with an application to time-lapse saturation and pressure changes from a $CO_2$ flood at Lost Hills, California. The approach was first implemented by Vasco et al. (2001), using surface deformation to estimate pressure changes within a shallow fracture zone and, ultimately, fracture zone permeability. In this study I examine how time-lapse pressure and saturation estimates can be used to image reservoir permeability variations.

## METHODOLOGY

In this section I describe the method used to estimate reservoir permeability from time-lapse data. The main idea is this: given the boundary conditions, well flow rates, and an estimate of reservoir pressure variations, one may estimate reservoir flow properties directly, by solving a linear inverse problem. Thus, a problem which appears to be inherently non-linear, estimating reservoir permeability from remote observations, can be rendered linear. The situation is the same in other geophysical inverse problems. For a majority of geophysical inverse problems the non-linearity is due to the presence of product terms in the governing differential equations These product terms contain an unknown field quantity which is multiplied by an unknown material property (Everett 1996, Vasco 2000). For example, in order to estimate permeability in the subsurface one must know the reservoir fluid pressure. However, the pressure field depends upon variations in reservoir permeability. If it were possible to estimate the pressure field independently, one could substitute the estimated field into the governing equation. The result would be a linear equation which may then be solved for reservoir permeability.

### Relationship between time-lapse changes and reservoir permeability

Here I consider reservoir pressure at two distinct times, $T_0$ and $T_1$, associated with two geophysical surveys. In what follows it will be assumed that the reservoir pressure is quasi-static with respect to the time scale of each time-lapse survey. That is, it will be assumed that for the duration of each survey, which is typically several hours to a day, the pressure is not changing dramatically. I shall also neglect capillarity and gravitational effects in order to simplify the treatment. It should be noted that both these effects may be considered, but including them would complicate this initial presentation. In the Appendix the necessary modifications for including gravity are given. Note that capillary effects are not significant for many important applications, such as waterflooding.

Consider an implicit pressure-explicit saturation (IMPRES) formulation of the governing equations for the evolution of reservoir saturation and fluid pressure (Peaceman 1977). Neglecting capillary and gravitational effects, the pressure in the oil phase, $P(\mathbf{x},t)$ is given by the solution of the equation (Crichlow 1977)

$$\nabla \cdot (K\lambda \nabla P) = Q \tag{1}$$

where $K(\mathbf{x})$ denotes the absolute permeability, $Q$ is a source term due to the boundary conditions, and $\lambda$ is the

total mobility, given by the sum of the mobilities

$$\lambda = \sum_j \frac{k_{rj}(S_j)}{\mu_j}. \tag{2}$$

i. e. a sum of the ratios of relative permeability $k_{rj}(S_j)$, which is a function of the saturation of the j-th phase $S_j$, and the viscosity of the $j$-th phase, $\mu_j$, If I consider the pressure field at two distinct times, $T_0$ and $T_1$, subject to distinct boundary conditions $Q_0$ and $Q_1$, respectively, the governing equations are

$$\nabla \cdot (K\lambda_0 \nabla P_0) = Q_0 \tag{3}$$

$$\nabla \cdot (K\lambda_1 \nabla P_1) = Q_1 \tag{4}$$

where $\lambda_0$ is the total mobility at time of the base seismic survey ($T_0$) and $\lambda_1$ is the total mobility at the time of the follow-up survey ($T_1$). Subtracting equation (3) from equation (4) he have

$$\nabla \cdot (K\lambda_1 \nabla P_1 - K\lambda_0 \nabla P_0) = Q_1 - Q_0. \tag{5}$$

Rearranging equation (5)

$$\nabla \cdot \left[ K\frac{(\lambda_1 + \lambda_0)}{2} \nabla P_\Delta + K\frac{(\lambda_1 - \lambda_0)}{2} (\nabla P_0 + \nabla P_\Delta) \right]$$

$$= Q_\Delta \tag{6}$$

where $P_\Delta$ denotes the change in reservoir pressure between time $T_0$ and $T_1$

$$P_\Delta = P_1 - P_0 \tag{7}$$

and similarly $Q_\Delta$ represents the change in boundary conditions from time $T_0$ to time $T_1$

$$Q_\Delta = Q_1 - Q_0. \tag{8}$$

The average total mobility is denoted by

$$\bar{\lambda} = \frac{\lambda_1 + \lambda_0}{2} \tag{9}$$

and the change in total mobility over the time interval is denoted by

$$\lambda_\delta = \frac{\lambda_1 - \lambda_0}{2}. \tag{10}$$

Equation (6) can be written more compactly in terms of the new variables

$$\nabla \cdot \left[ K\bar{\lambda} \nabla P_\Delta + K\lambda_\delta (\nabla P_0 + \nabla P_\Delta) \right] = Q_\Delta. \tag{11}$$

Using the definition

$$\mathbf{\Phi} = \bar{\lambda} \nabla P_\Delta + \lambda_\delta (\nabla P_0 + \nabla P_\Delta) \tag{12}$$

equation (11) takes the very concise form

$$\nabla \cdot (K\mathbf{\Phi}) = Q_\Delta \tag{13}$$

or, carrying out the differentiation,

$$\nabla K \cdot \mathbf{\Phi} + K \nabla \cdot \mathbf{\Phi} = Q_\Delta \tag{14}$$

a first-order, linear partial differential equation for $K(\mathbf{x})$.

Given an estimate for $\mathbf{\Phi}$ within the reservoir, and appropriate boundary conditions for $K(\mathbf{x})$, equation (14) can be solve numerically for the permeability variations within the reservoir. That is, I write equation (14) in discrete form using finite differences,

$$\sum_{n=1}^{N} \kappa_{jn} K_n = Q_j \qquad j = 1, N \tag{15}$$

where $\kappa_{jn}$ and the discrete versions of the coefficients in (14), $Q_j$ are the discretized source terms, and $N$ is the number of grid blocks in the reservoir model. Equation (15) may be solved for $K(\mathbf{x})$ using a sparse matrix solver such as the LSQR algorithm (Paige and Saunders 1982) or a related conjugate gradient solver (Seager 1989). Note that, as indicated in the Appendix, one retains the form of equation (14) when gravity is also included [equation (A14)]. As noted by Vasco (2000), the governing differential equation may be transformed into an equivalent integral expression using the method of weighted residuals (Finlayson 1972). The integral may be approximated as a discrete sum by expanding the quantities in a set of orthogonal basis functions (Parker 1994). I can then solve the system of equations for reservoir permeabilities using any linear solver. In addition, one typically regularizes the system of equations through the addition of model norm and roughness penalty constraints, as discussed in Parker (1994).

**Estimating $\mathbf{\Phi}$ from time-lapse observations**

In order to compute $\mathbf{\Phi}$ it is necessary to estimate the average total mobility ($\bar{\lambda}$), the change in total mobility ($\bar{\lambda}$), the background pressure ($P_0$), and the change in reservoir pressure ($P_\Delta$). Time-lapse observations provide estimates of changes in both saturation and pressure as described in Tura and Lumley (1998) and Landro (2001). Thus, time-lapse observations only constrain changes in the state of the reservoir and it is necessary to estimate the background saturation and pressure by other means.

In the simple case of single phase flow, the total mobility is constant in both space and time. Thus, $\lambda_\delta$ vanishes, $\bar{\lambda}$ is a known constant and I may determine $P_\Delta$ from the time-lapse seismic pressure estimates alone. Such considerations also apply if the phase mobilities are similar in value. Therefore, in favorable situations such as primary production, well testing, and injection of a phase

with similar mobility, I can apply the methodology directly. Such was the situation for the shallow pumping test analyzed in Vasco et al. (2001).

Even when the phase mobilities vary significantly equation (14) may be used to estimate reservoir permeability. Specifically, in regions or zones where the saturations have not changed, such as ahead of an encroaching water front, one can estimate $\mathbf{\Phi}$ from the time-lapse data. In portions of the reservoir where the saturation has changed, such as behind a water front, one can use the saturation changes to estimate the permeability directly (Vasco et al. 2003). In these regions the permeabilities may then be held fixed at their estimated values, as a boundary condition, while equation (14) is used to find the permeabilities in portions of the reservoir in which there have been no saturation changes. Alternatively, in certain circumstances, such as water floods one might neglect the mobility change associated with the advancing water and set $\lambda_1$ equal to $\lambda_0$ in (9) and (10). This is a crude approximation, but, as I shall show in the analysis of synthetic time-lapse changes below, for early times the mobility change is only significant near the water injectors.

In a number of situations it is possible to either estimate or approximate the initial reservoir saturations and pressure. For example, it may be possible to use seismic reflection data to estimate the initial pressure distribution (Reynolds 1970, Martinez et al. 1991). Such data might be coupled with observations of downhole pressure made prior to production. Seismic data can often image the initial water-oil contact which may be used to estimate initial saturations and mobilities. Alternatively, it is often possible to construct a reservoir model and compute the initial conditions of the reservoir prior to production. The time-lapse observations can then be used to compute the changes in pressure and saturation, which are subsequently added to the initial values. Thus, one approximates the initial reservoir pressure distribution, $P_0$, and the initial saturations ${S^0}_j$ and uses the time-lapse information to estimate the changes. For the special case in which initial pressure is constant throughout the the reservoir, the term $\nabla P_0$ vanishes identically and only the average total mobilities $\bar{\lambda}$ and the change in pressure are needed.

## APPLICATIONS

As an illustration I apply the methodology to a set of synthetic pressure and saturation changes. This test case mimics a time-lapse three-dimensional seismic survey of a waterflood. In addition, I describe an application of the technique to observations from an oil field at Lost Hills, California.

### Synthetic Time-Lapse Changes

The reference permeability model used to generate the reservoir pressure and saturation changes is shown in Figure 1. A 53 by 18 cell grid is used to describe the reservoir permeability structure. The values have been interpolated onto a finer grid for display purposes. The single-layer model is characterized by higher permeabilities in the central and eastern portions of the reservoir. Overall, lower permeabilities are found to the west and the north-east in this reference structure.

A reservoir simulator was used to compute the saturation and pressure changes associated with 1000 days of production. Five producing wells, indicated by open circles in Figure 1, are located near the southern edge of the model. The five producing wells are constrained to maintain a pressure of 5000 psi. A single water injector, denoted by a star in Figure 1, is located near the northern boundary of the model. Water is injected into the reservoir interval at a rate of 400 barrels per day. No flow boundary conditions are maintained at the edges of the model. The initial reservoir pressure is a uniform 6860 psi and the initial water saturation is 0.09. The water saturation changes after approximately one year is shown in Figure 2. For the most part, the water is migrating along the central high permeability channel from the northern injector to the south-eastern producers. The total mobility after 360 days is also shown in Figure 2. The significant change in total mobility is concentrated near the water injector, in most of the reservoir the total mobility is close to the background value of 0.19 $\mathrm{cP}^{-1}$.

After 360 days of production, the reservoir pressure near the five producers has decreased from 6860 psi to values approaching 5000 psi (Figure 3). The pressure is highest, approximately 5500 psi, surrounding the water injector to the north. The influence of the heterogeneity is visible in Figure 3, the pressure changes are skewed by the higher permeabilities in the center of the model. The magnitude of the pressure gradient is displayed in Figure 4, along with the magnitude of the vector quantity $\mathbf{\Phi}$, given by equation (12). The pressure gradient and divergence were computed using bicubic splines (De Boor 1978). The vector $\mathbf{\Phi}$ is the fundamental quantity upon which the coefficients of the differential equation for $K(\mathbf{x})$, equation (14), depend. Note the similarity of the pressure gradient magnitude and the magnitude of $\mathbf{\Phi}$ in Figure 4. Because the background pressure $P_0$ is constant, its gradient vanishes and (12) is only a function of the gradient of the pressure change, $\nabla P_\Delta$, and the total mobility at time $T_1$. From Figure 2 it is clear that the total mobility at time $T_1$ is only significant near the water injector.

In order to set up and solve the differential equation (14) I must estimate the coefficients, which depend on $\mathbf{\Phi}$, the source term $Q_\Delta$ , which depends on the flow rates at the wells, and boundary values for $K$. The components of $\mathbf{\Phi}$ depend on the spatial gradient of $P_\Delta$ [equation (12)]

and the total mobility at time $T_1$, which may be estimated from the time-lapse saturation change or approximated from the initial saturation distribution. The components of $Q_\Delta$, the flow rates at the two times ($T_0$ and $T_1$), are determined directly, from measurements made at the wells.

Because (14) is a first order differential equation for $K$, I need to have boundary values for the permeabilities in order to solve it. In some circumstances, for example in a crosswell setting, one might have estimates of permeability at the edges of the grid. Alternatively, the edge of the model might coincide with a natural boundary, such as a fault, where estimates of the permeability are available. However, in general one does not know a priori the permeability at the model boundary. In such situations it is necessary to set the boundary permeability to an estimated value. For the synthetic test I set the boundary permeability values to 100 milli-Darcies as an initial guess.

Given the coefficients, the source term, and the boundary values for $K$, equation (14) may be solved for the permeability distribution within the reservoir. To do this I use the sparse matrix linear system solver LSQR (Paige and Saunders 1982). This iterative solver simply requires sparse matrix-vector multiplications and converges quite rapidly, reducing the misfit to a small value in just a few iterations (Figure 5). Note that the final error is not exactly zero. This is most likely due to the use of inexact boundary values for the permeability in solving equation (14). Also, the total mobility values of the background saturation distribution, and not the final saturation distribution, were used in computing $\mathbf{\Phi}$. This introduces an additional error in the coefficients of the differential equation (14). The entire calculation took under 0.1 CPU seconds on a PC. The resulting permeability estimates are shown in Figure 6. The general features of the reference model are reproduced in the estimated distribution of $K$. In particular, a central high permeability channel is recovered, extending roughly north-south to northwest-southeast. Also, the eastern high permeability region is reproduced by the inversion. Lower permeabilities are found in the western portion of the reservoir model, in agreement with our reference values. Overall, the large-scale features of the reference model are recovered in spite of the fact that the boundary values were initially set to a nominal value of 100 milli-Darcies. As noted above, the permeability estimates result from the solution of the linear equation (14). Thus, the estimates are obtained directly and the solution is not plagued by non-uniqueness due to the choice of a starting model.

### A $CO_2$ Injection at Lost Hills, California

**Overview.**—The Lost Hills field in California has undergone extensive water-flooding since 1995. The time-lapse data were gathered as part of a pilot study to demonstrate how $CO_2$ injection can enhance oil recovery in the diatomite. The diatomite is a low permeability, high porosity formation containing a considerable amount of oil in place. Because of the low permeability it is difficult to access the large volume of oil in the formation. Time-lapse crosswell seismic and electromagnetic (EM) surveys were conducted in order to better understand how oil and $CO_2$ migrate through the diatomite.

The general setup of the imaging experiment is shown in Figure 7. An injection well, 11-8WR, is located near two fiberglass-cased observations wells. During the fall, winter, and spring of 2000-2001 $CO_2$ was injected into 11-8WR, at an average rate of 104 $m^3/s$. Two sets of crosswell surveys were conducted between observation wells OB-C1 and OB-C2. Baseline surveys were completed in September 2000, before the start of $CO_2$ injection. A follow-up EM survey was run in April 2001 and an additional seismic survey was concluded in May 2001. In January of 2001 the two observation wells were relogged for electrical resistivity.

**Estimating Saturation and Pressure Changes.**—The first step in the estimation of permeability is to determine the pressure and saturation changes within the reservoir due to injection and production (Hoversten et al. 2003). This was not a trivial undertaking, given the rather involved oil recovery process. That is, there are three, possibly four, phases is the reservoir: water, oil, $CO_2$ and perhaps hydrocarbon gas. Thus, there is both miscible and immiscible flow at Lost Hills. Furthermore, there are a number of variables needed to characterize the state of the reservoir: the saturations of the four phases and the pore pressure. Here I simply outline the procedure used to estimate the changes in pore fluid content and pressure, more detail may be found in Hoversten et al (2003).

Several rock physics models were required in order to interpret the EM and seismic survey results in terms of fluid saturations and pressure. These models included Gassmann's equation (Gassmann 1951), Archie's relationship (Archie 1942), Wood's mixing formula (Wood 1955), and Hertz-Mindin contact theory (Dvorkin and Nur 1996). The rock physics models were calibrated using well log estimates of porosity, water and gas saturation and core data (Bilodeau 1995, Hoversten et al. 2003). Reference water saturation ($S_w$=0.5) and porosity ($\phi$=0.52) were determined from averages in well OB-C1 in the reservoir prior to $CO_2$ injection. The initial model of conductivity was also derived from well logs.

The baseline crosswell EM survey provided an estimate of conductivity variations between the wells. This baseline conductivity structure was the starting model for an inversion of data from the follow-up EM survey. Bulk electrical conductivity changes $\sigma_{bulk}$, derived from time-lapse crosswell EM data, are used to infer changes in water saturation, $S_w$ based upon Archie's (1942) relationship

$$\sigma_{bulk} = \sigma_{brine} \cdot \phi^m \cdot {S_w}^n \qquad (16)$$

where $\sigma_{brine}$ is the fluid conductivity, $\phi$ is the porosity, and $m$ and $n$ are numbers between 1 and 3. The resulting estimates of the changes in water saturation during the $CO_2$ injection are shown in Figure 8. Overall, there is a decrease in water saturation as $CO_2$ is injected into well 11-8WR. The $CO_2$ was injected in narrow, one meter perforated intervals, which are indicated by open circles in Figure 8. The injection well was approximately 6 meters out of the crosswell plane but a hydro-fracture may extend from injector across the crosswell plane. The water saturation appears to undergo the largest decreases near the top and bottom of the interwell region and in three horizontal zones near the upper four injection perforations. With the exception of the lowermost right-hand corner, the decrease in water saturation is less than 30%.

The next step involves estimating the change in reservoir pressure as the injection proceeded. Pressure changes are significant at Lost Hills because it is a shallow reservoir and the host rock, the diatomite, is notably effected by pressure (Hoversten et al. 2003). The initial reservoir pressure was calculated from a reservoir simulation of the six years of water injection (Hoversten et al. 2003). Estimates of pressure change are derived from shear velocity ($V_s$) tomograms resulting from an inversion of the shear wave arrival times. The shear velocity $V_s$ is a very weak function of fluid saturation and is primarily influenced by pressure changes within the reservoir (Tura and Lumley 1998). Even so, the EM crosswell data do provide estimates of $S_w$ changes which are combined with changes in $V_s$ to compute reservoir pressure changes (Figure 9). There is an increase in reservoir pressure due to the injection of $CO_2$ in well 11-8WR. However, the pressure increase is non-uniform over the crosswell plane. Several regions around the $CO_2$ injection intervals undergo large pressure changes.

Finally, compressional velocity ($V_p$) changes, corrected for pressure and water saturation effects, are used to determine changes in $CO_2$ saturation. This step involves additional assumptions concerning the amount of hydrocarbon gas in the reservoir (Hoversten et al. 2003). I merely show the results of the Hoversten et al. (2003) inversion for the ratio of $CO_2$ to oil in the reservoir (Figure 8). The working assumption of the reservoir engineers in the Lost Hills is that the injected $CO_2$ immediately dissolves into the oil in place (Hoversten et al. 2003). The presence of the $CO_2$ will modify the density and viscosity, and hence the mobility, of the contacted oil (Stalkup 1983).

**Permeability.**—Using the estimated pressure and saturation changes between the boreholes I compute the components of $\mathbf{\Phi}$ given by equation (12). The computation of the total mobility requires some modification due to the presence of the $CO_2$ in the reservoir. The $CO_2$ gas and oil are considered miscible components of the non-wetting oil phase (Todd and Longstaff 1972). The relative permeabilities of the oil and $CO_2$ gas in the oil and gas mixture are given by

$$k_{ro} = \frac{S_o}{S_n} k_{rn} \tag{17}$$

$$k_{rCO_2} = \frac{S_{CO_2}}{S_n} k_{rn}$$

where $S_n = S_o + S_{CO_2}$ is the non-wetting phase saturation and $k_{rn} = k_{rn}(S_w)$ is the imbibition relative permeability of the non-wetting phase (Todd and Longstaff 1972). The effective viscosities of the oil and $CO_2$ gas in the mixture are given by the empherical formulas

$$\mu_{oe} = {\mu_o}^{1-\omega} {\mu_m}^{\omega} \tag{18}$$

$$\mu_{CO_2 e} = {\mu_{CO_2}}^{1-\omega} {\mu_m}^{\omega}$$

where $\mu_o$ and $\mu_{CO_2}$ denotes the viscosities of the unmixed phases and $\omega$ is a parameter describing the degree of mixing within a grid block. The quantity $\mu_m$ is the mixture viscosity, given by

$$\mu_m = \frac{\mu_o \mu_{CO_2}}{\left(S_{CO2}/S_n {\mu_o}^{1/4} + S_o/S_n {\mu_{CO_2}}^{1/4}\right)^4} \tag{19}$$

(Todd and Longstaff 1972). The total mobility for the water-oil-$CO_2$ mixture is then given by

$$\lambda = \frac{k_{rw}(S_w)}{\mu_w} + \frac{k_{ro}(S_w)}{\mu_o} + \frac{k_{rCO_2}(S_w)}{\mu_{CO_2}} \tag{20}$$

where $S_w$ and the ratio of $CO_2$ to oil estimated from the EM and seismic surveys are used in equations (18), (19), and (20).

All the quantities required to calculate $\mathbf{\Phi}$ are now at hand: the background pressure, the pressure change, the total mobility estimates from the pre-injection and follow-up surveys. Thus, I can construct the differential equation (14) for permeability within the reservoir. Boundary conditions are also needed to solve equation (14) uniquely. That is, I am required to specify the permeability at the boundaries of the crosswell region. In addition, the iterative numerical solver converges more rapidly if an initial estimate of $K(\mathbf{x})$ is available (Seager 1989). Fortunately, a permeability log is available for observation well OB-C1, at the left side of the interwell region (Figure 10). The log was used to set up an initial layered permeability model. Hence, I have specified the differential equation, the boundary conditions, and a starting model for the iterative solver.

The numerical grid used to represent the permeability variations is identical to that used to define the saturations and pressure variations (Figures 8 and 9). The mesh is 17 grid blocks (lateral) by 141 grid blocks (vertical) for a total of 2397 unknown permeability values. The grid blocks are 1.4 m laterally by 1.5 m vertically. The LSQR algorithm (Paige and Saunders 1982) is used to solve the

linear system which results from using finite-differences to approximate equation (14). The error reduction as a function of the number of iterations is shown in Figure 11. The error is reduced by about 98% in just 1.8 CPU seconds on a PC. The resulting permeability model is displayed in Figure 12. In general, permeabilities are higher at the top of the model and lower near the bottom edge. There are a number of sub-horizontal high permeability zones crossing the interwell region. Also, there is a band of higher permeabilities extending from the left side of the model, at a depth of about 550 m, to the right side, around 520 m. Note that the permeabilities, while low overall, are quite variable within the interwell region. In particular, the pattern of permeability changes significantly over a distance of ten meters or more.

As a check on the estimated permeabilities I compare values of $K$ in column 13 of the model with the logged permeabilities from well 11-8WR (Figure 13). If well 11-8WR is projected onto the crosswell plane it would coincide with column 13 of the model. From Figure 13 we observe an overall correlation between the well log estimates of $K$ and the crosswell estimates. There are higher permeabilities at the top of the model and lower permeabilities at the base. There are differences in detail however, which may be due to the six meters of separation between the actual location of 11-8WR and its projection onto the crosswell plane. As is evident in Figure 12, the permeabilities can change noticeably over such distances.

It is interesting to relate the estimated permeability variations to the computed saturation changes in Figure 8. For example, large decreases in water saturation coincide with sub-horizontal bands of high permeability just above the top-most injection interval and just below the second injection interval (Figure 12). There is also a slightly dipping band of $S_w$ decrease between the third and fourth water injector which correlates with a dipping zone of high permeability. $CO_2$ saturation changes also correlate with higher permeability regions though the pattern is quite different when compared to the water saturation changes. There may be gravitational effect which promotes more vertical movement of the $CO_2$ in the reservoir. It seems that the $CO_2$ may be migrating up high permeability pathways. This is particularly evident when the $CO_2$ saturation change is plotted as a percent of the maximum possible value for a given pressure and temperature (Hoversten et al. 2003).

## CONCLUSIONS

In many situations time-lapse geophysical data can be used to image reservoir flow properties. For example, if one can approximate the initial conditions of the reservoir, time-lapse seismic observations can be used to infer saturation and pressure changes. It is a linear inverse problem to infer reservoir permeability variations from the time-lapse estimated saturation and pressure changes, as indicated by equation (14). The linearity of the inverse problem is a significant advantage. Computationally it is not necessary to repeatedly linearize and iterate in the hope of converging to a solution. Rather, one can solve the linear problem directly and estimate permeabilities within the reservoir quite efficiently, in a matter of a few seconds for the applications described here.

In the approach outlined here, techniques from linear inverse theory may be used to characterize the non-uniqueness. As an example, consider the calculation of model parameter resolution. First, write either equation (14) or (15) in vector-matrix form

$$\mathbf{MK} = \mathbf{Q} \tag{21}$$

where $\mathbf{M}$ is a matrix of coefficients such as $\kappa_{jn}$ in (15), $\mathbf{K}$ is the vector containing the reservoir permeabilities and $\mathbf{Q}$ is a vector containing the terms on the right-hand-side of equation (14) or (15). An estimate of reservoir permeabilities, $\hat{\mathbf{K}}$, is given by

$$\hat{\mathbf{K}} = \mathbf{M}^{\dagger}\mathbf{Q} \tag{22}$$

where $\mathbf{M}^{\dagger}$ denotes the generalized inverse of $\mathbf{M}$ (Aki and Richards 1980). The resolution matrix, $\mathbf{R}$, which relates the estimated permeabilities $\hat{\mathbf{K}}$ to a hypothetical set of true permeabilities $\mathbf{K}$ is obtained by substituting equation (21) into equation (22)

$$\hat{\mathbf{K}} = \left[\mathbf{M}^{\dagger}\mathbf{M}\right]\mathbf{K} = \mathbf{RK}. \tag{23}$$

Thus, one can calculate the resolution of reservoir permeabilities directly. Note that the resolution matrix is not independent of the data in this case, because elements of $\mathbf{\Phi}$ are contained in the coefficients of the matrix $\mathbf{M}$.

The methodology presented here is new and the applications are preliminary but the results are encouraging. The technique does depend on estimates of reservoir pressure changes derived from geophysical observations such as time-lapse seismic data. As such, the results will depend on the accuracy of these estimates. Errors in the saturation and pressure estimates, such as leakages from pressure estimates into saturation estimates (Landro 2001) will impact the calculated permeabilities. It will be useful to combine downhole well pressure data with time-lapse seismic observations in a coupled inversion. This approach proved fruitful in combining surface tilt and well pressure observations to estimate permeability variations in a shallow fracture zone (Vasco et al. 2001). Given the increasing availability of downhole pressure observations from horizontal wells, the coupled inversion could significantly improve estimates of reservoir permeability. The downhole pressure observations will provide a valuable calibration of the time-lapse seismic estimates.

## ACKNOWLEDGMENTS

This work was supported by the Assistant Secretary for Fossil Energy, Office of Oil Gas and Shale Technologies, of the U.S. Department of Energy under contract DE-AC03-76SF00098. I wish to thank G. M. Hoversten for providing the estimates of pressure and saturation changes associated with the Lost Hills time-lapse crosswell surveys. I also wish to thank the Chevron Petroleum Co., in particular Mike Morea, for providing data from Lost Hills. All computations were carried out at the Center for Computational Seismology.

## REFERENCES

Aki, K., and Richards, P. G., 1980, *Quantitative Seismology*:, W. H. Freeman and Co., San Francisco, California.

Archie, G. E., 1942, The electrical resistivity log as an aid in determining some reservoir characteristics, *Trans. Am. Inst. Mech. Eng.*, **146**, 54-62.

Bahorich, M. S., and Farmer, S. L., 1995, 3-D seismic discontinuity for faults and stratigraphic features: *The Leading Edge*, **14**, 1053-1058.

Bilodeau, B. J., 1995, Determining water saturation in diatomite using wireline logs, Lost Hills Field, California, *SPE Proceedings of the Western Regional Meeting*, SPE29653, Bakersfield, CA, 369-382.

Bratvedt, F., Gimse, T., and Tegnander, C., 1996 Streamline computations for porous media flow including gravity: *Transport in Porous Media*, **25**, 63-78.

Brevik, I., 1999, Rock model based inversion of saturation and pressure changes from time lapse seismic data: *69th Ann. Internat. Mtg. Soc. Expl Geophys.*, Expanded Abstracts, 1044-1047.

Cohen, I., and Coifman, R. R., 2002, Local discontinuity measures for 3-D seismic data, *Geophysics*, **67**, 1933-1945.

Crichlow, H. B., 1977, *Modern Reservoir Engineering*:, Prentice Hall, New Jersey.

De Boor, C., 1978, *A Practical Guide to Splines*:, Springer-Verlag, New York.

Everett, M. E., 1996, Homotopy, polynomial equations, gross boundary data, and small Helmholtz systems, *J. Comp. Phys.*, **124**, 431-441.

Dvorkin, J., and Nur, A., 1996, Elasticity of high-porosity sandstones: Theory for two North Sea datasets: *Geophysics*, **61**, 1363-1370.

Finlayson, B. A., 1972, *The Method of Weighted Residuals and Variational Principles*:, Academic Press, New York.

Gassmann, F., 1951, Elastic waves through a packing of spheres: *Geophysics*, **16**, 673-685.

Gersztenkorn, A., and Marfurt, K., 1999, Eigenstructure-based coherence computations as an aid to 3-D structural and stratigraphic mapping: *Geophysics*, **64**, 1468-1479.

He, W., Guerin, G., Anderson, R. N., and Mello, U. T., 1998, Time-dependent reservoir characterization of the LF sand in the South Eugene Island 330 Field, Gulf of Mexico: *The Leading Edge*, **17**, 1434-1438.

Huang, X., Meister, L., and Workman, R., 1998, Improving production history matching using time-lapse seismic data: *The Leading Edge*, **17**, 1430-1433.

Hoversten, G. M., Gritto, R., Washbourne, J. and Daley, T., 2003, Pressure and fluid saturation prediction in a multicomponent reservoir, using combined seismic and electromagnetic imaging, *Geophysics*, (submitted).

Jack, I. C., 1997, *Time-lapse Seismic in Reservoir Management*:, Society of Exploration Geophysicists, Tulsa.

Landa, J. L., and Horne, R. N., 1997, A procedure to integrate well test data, reservoir performance history, and 4-D seismic information into a reservoir description: paper SPE 38653 presented at the 1997 SPE Annual Technical Conference and Exhibition, San Antonio, Texas, October 5-8.

Landro, M., 2001, Discrimination between pressure and fluid saturation changes from time-lapse seismic data: *Geophysics*, **66**, 836-844.

Martinez, R. D., Schroeder, J. D. and King, G. A., 1991, Formation pressure prediction with seismic data from the Gulf of Mexico, *Form. Eval.*, **3**, 27-32.

Paige, C. C., and Saunders, M. A., 1982, LSQR: An algorithm for sparse linear equations and sparse linear systems: *ACM Trans. Math. Software*, **8** , 195-209.

Parker, R. L., 1994, *Geophysical Inverse Theory*:, Princeton Univ. Press, Princeton, N. J.

Peaceman, D. W., 1977, *Fundamentals of Numerical Reservoir Simulation*:, Elsevier Scientific Publishing.

Reynolds, E. B., 1970, Predicting overpressured zones with seismic data: *World Oil*, **171**, 78-82.

Seager, M. K., 1989, A SLAP for the masses, in *Parallel Supercomputing: Methods, Algorithms, and Applications,*, G. F. Carey (Ed.), 135-155.

Stalkup, F. I., 1983, *Miscible Displacement*:, SPE Monograph Series, New York.

Todd, M. R., and Longstaff, W. J., 1972, The development, testing, and application of a numerical simulator for predicting miscible flood performance, *J. Pet. Tech.*, **253**, 874-882.

Tura, A., and Lumley, D. E., 1998, Subsurface fluid-flow properties from time-lapse elastic-wave reflection data: *SPIE Proceedings*, 43rd Annual Meeting, 125-138.

Vasco, D. W., 2000, An algebraic formulation of geophysical inverse problems, *Geophys. J. Int.*, **142**, 970-990.

Vasco, D. W., Karasaki, K. and Kishida, K., 2001, A coupled inversion of pressure and surface displacement: *Water Resour. Res.*, **37**, 3071-3089.

Vasco, D. W., Datta-Gupta, A., Behrens, R., Condon, P., and Rickett, J., 2003, Seismic imaging of reservoir properties: Time-lapse amplitude changes: *Geophysics* (submitted).

Wood, A. W., 1955, *A Textbook of Sound*:, The MacMillan Co., New York.

Yilmaz, O., 2001, *Seismic Data Analysis, Volume II*:, Society of Exploration Geophysicists, Tulsa.

## APPENDIX: MODIFICATIONS FOR GRAVITY

In this Appendix gravitational effects are included in the formulation. As in equation (1), a quasi-static formulation will be considered. That is, it will be assumed that the densities of the fluids do not change significantly over the duration of each geophysical survey. In place of equation (1), the modified governing equation is (Bratvedt et al. 1996)

$$\nabla \cdot (K\lambda \nabla P) - \nabla \cdot (K\Lambda \mathbf{g}) = Q \qquad (A1)$$

where $K(\mathbf{x})$ denotes the absolute permeability, $Q$ is a source term due to the boundary conditions, and $\lambda$ is the total mobility, given by the sum of the mobilities

$$\lambda = \sum_j \frac{k_{rj}(S_j)}{\mu_j}. \qquad (A2)$$

and the relative permeability $k_{rj}(S_j)$, is a function of the saturation of the j-th phase $S_j$, and the viscosity of the $j$-th phase, $\mu_j$. The quantity $\Lambda$ is the sum of the mobilities weighted by the phase densities, $\rho_j$,

$$\Lambda = \sum_j \rho_j \frac{k_{rj}(S_j)}{\mu_j}. \qquad (A3)$$

As above, I consider the state of the reservoir at two times, $T_0$ and $T_1$, corresponding to the times of the baseline and follow-up geophysical surveys, respectively. At each time the saturations and pressure in the reservoir will vary. Thus, for time $T_0$ one has the equation

$$\nabla \cdot (K\lambda_0 \nabla P_0) - \nabla \cdot (K\Lambda_0 \mathbf{g}) = Q_0 \qquad (A4)$$

while at time $T_1$ one has

$$\nabla \cdot (K\lambda_1 \nabla P_1) - \nabla \cdot (K\Lambda_1 \mathbf{g}) = Q_1. \qquad (A5)$$

Subtracting equation (A4) from (A5) and making use of the definitions

$$P_\Delta = P_1 - P_0 \qquad (A6)$$

$$Q_\Delta = Q_1 - Q_0 \qquad (A7)$$

$$\bar{\lambda} = \frac{\lambda_1 + \lambda_0}{2} \qquad (A8)$$

$$\lambda_\delta = \frac{\lambda_1 - \lambda_0}{2}. \qquad (A9)$$

$$\Lambda_\delta = \Lambda_1 - \Lambda_0 \qquad (A10)$$

we have

$$\nabla \cdot \left[K\bar{\lambda}\nabla P_\Delta + K\lambda_\delta(\nabla P_0 + \nabla P_\Delta) - K\Lambda_\delta \mathbf{g}\right] = Q_\Delta. \qquad (A11)$$

As above, we may define the vector quantity $\mathbf{\Phi}_g$

$$\mathbf{\Phi}_g = \bar{\lambda}\nabla P_\Delta + \lambda_\delta(\nabla P_0 + \nabla P_\Delta) + \Lambda_\delta \mathbf{g} \qquad (A12)$$

equation (A11) takes the very concise form

$$\nabla \cdot (K\mathbf{\Phi}_g) = Q_\Delta \qquad (A13)$$

or, carrying out the differentiation,

$$\nabla K \cdot \mathbf{\Phi}_g + K\nabla \cdot \mathbf{\Phi}_g = Q_\Delta \qquad (A14)$$

which has the same form as equation (14). The additional information which is required when gravity is included are the densities for the various phases.

## FIGURE CAPTIONS

**Figure 1.** Reference permeability model used to compute synthetic time-lapse saturation and pressure changes. Six pressure constrained producing wells are indicated by open circles. A single water injector is denoted by an open star.

**Figure 2.** (Top) Water saturation ($S_w$) within the reservoir after 360 days of production. (Bottom) Total mobility due to the distribution of water and oil within the reservoir at 360 days into production.

**Figure 3.** Reservoir pore pressure after 360 days of water injection and oil production.

**Figure 4.** (Top) The magnitude of the pressure gradient vector for the pressure distribution in Figure 3. (Bottom) The magnitude of the vector $\mathbf{\Phi}$ [equation (12)] associated with the pressure and saturation changes within the reservoir.

**Figure 5.** Total error as a function of the number of step of the iterative LSQR algorithm.

**Figure 6.** Estimate of reservoir permeabilities resulting from the numerical solution of equation (14).

**Figure 7.** Experimental set-up for the Lost Hills $CO_2$ injection. The observation wells used in the crosswell electromagnetic and seismic surveys are denoted by filled squares. The water injector 11-8WR is indicated by an open circle.

**Figure 8.** (Left) Estimate of water saturation ($S_w$) changes due to the injection of $CO_2$ in well 11-8WR. The $CO_2$ injection perforations are indicated with the open circles. (Right) Ratio of $CO_2$ to oil after the injection of $CO_2$ in well 11-8WR.

**Figure 9.** (Left) Estimated reservoir pressure prior to the injection of $CO_2$. (Right) Pore pressure changes due to the injection of $CO_2$.

**Figure 10.** Permeability logs for wells OB-C1 and 11-8WR. The wells logs have been smoothed using a 20 point moving average.

**Figure 11.** Total error as a function of the number of iterations of the LSQR linear system solver.

**Figure 12.** Estimates of reservoir permeabilities in the interwell region.

**Figure 13.** (Solid line) Permeability log for injection well 11-8WR. (Dashed line) Permeability estimates for column 13 in the model shown in Figure 12. This column corresponds to the projection of well 11-8WR onto the crosswell plane.

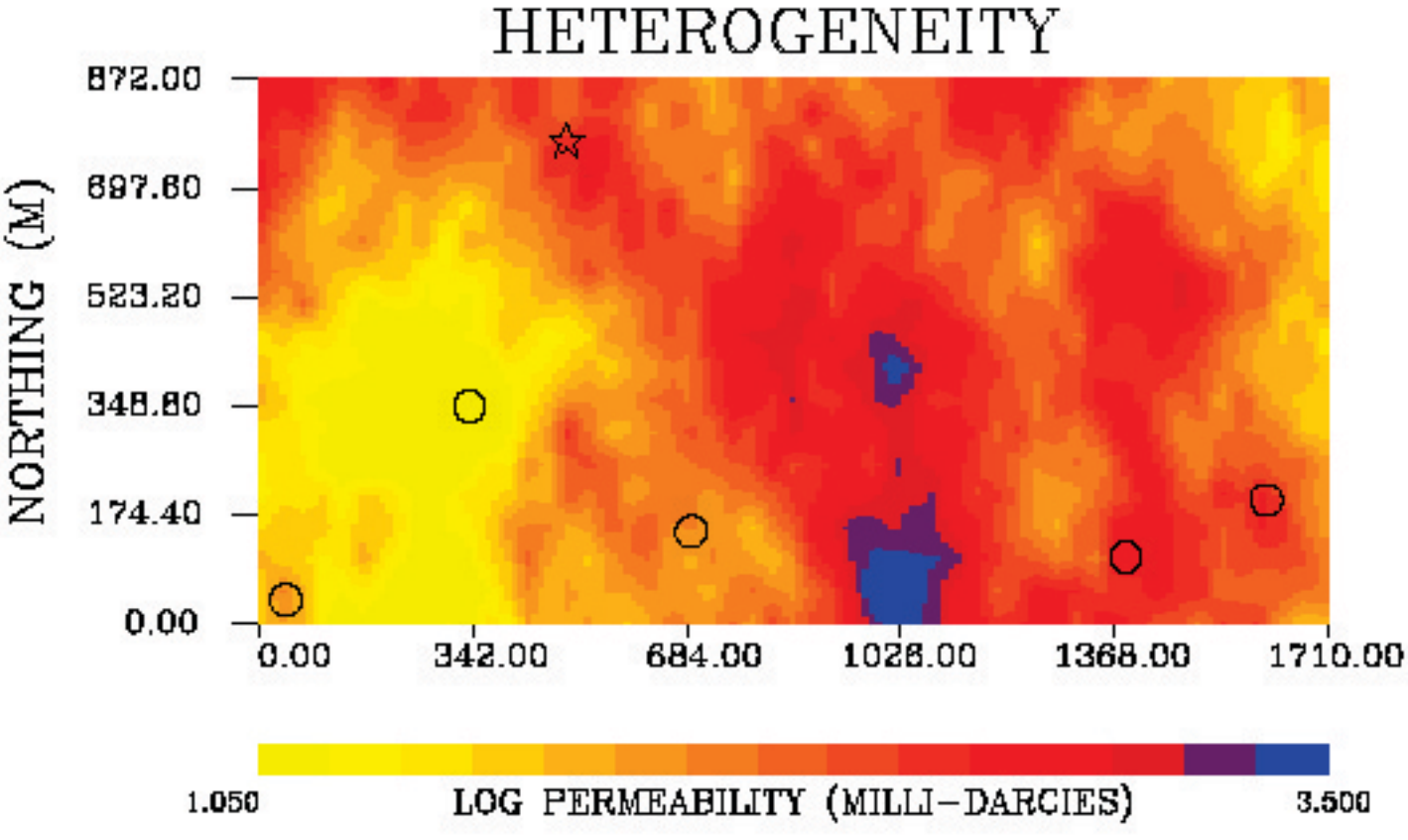
HETEROGENEITY
NORTHING (M)
872.00
697.60
523.20
348.80
174.40
0.00
0.00
342.00
684.00
1026.00
1368.00
1710.00
1.050
LOG PERMEABILITY (MILLI-DARCIES)
3.500

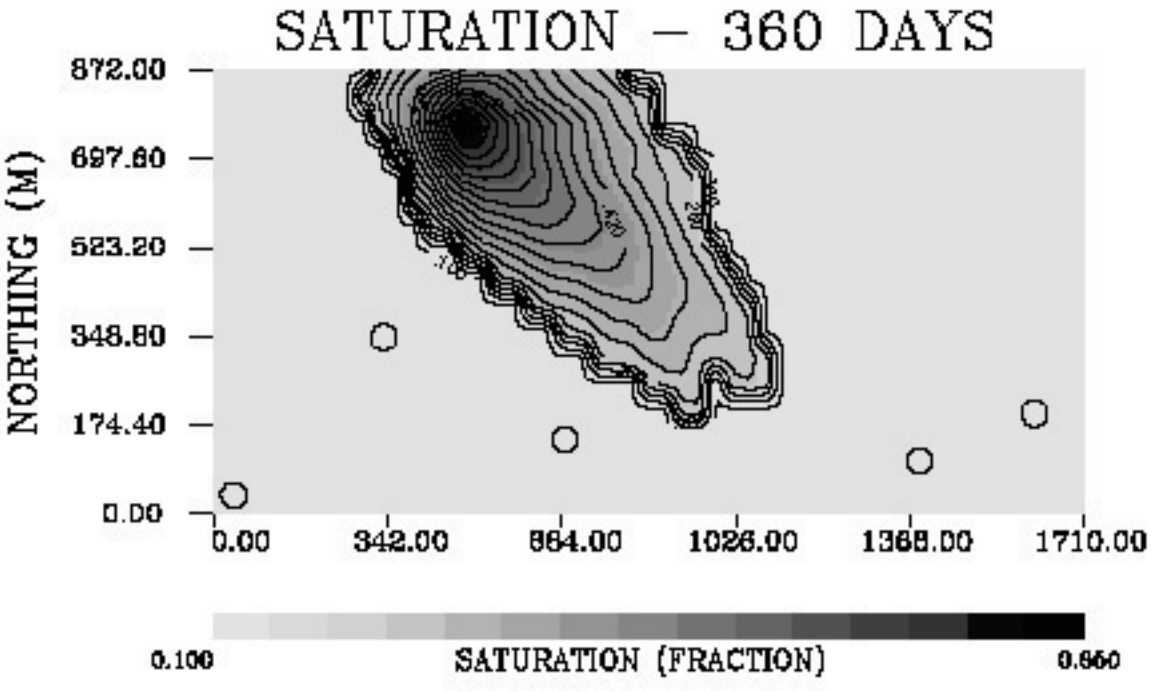
SATURATION – 360 DAYS
872.00
697.60
523.20
348.80
174.40
0.00
NORTHING (M)
0.00
342.00
684.00
1026.00
1368.00
1710.00
0.100
SATURATION (FRACTION)
0.950

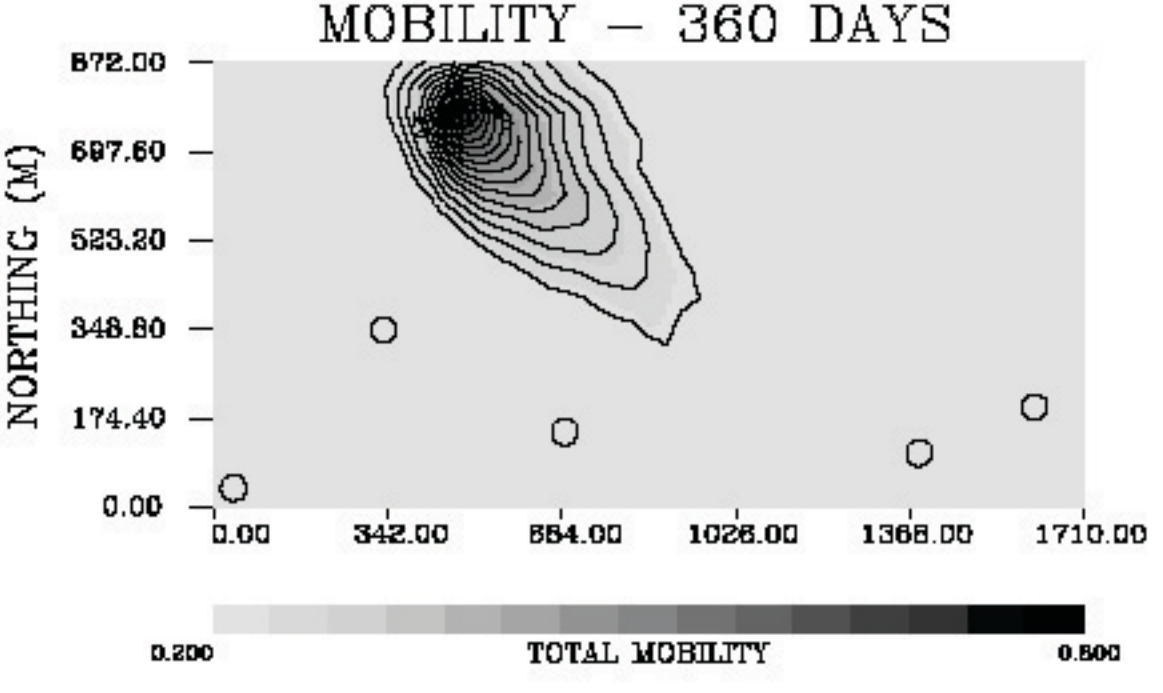
MOBILITY – 360 DAYS
872.00
697.60
523.20
348.80
174.40
0.00
NORTHING (M)
0.00
342.00
684.00
1026.00
1368.00
1710.00
0.200
TOTAL MOBILITY
0.800

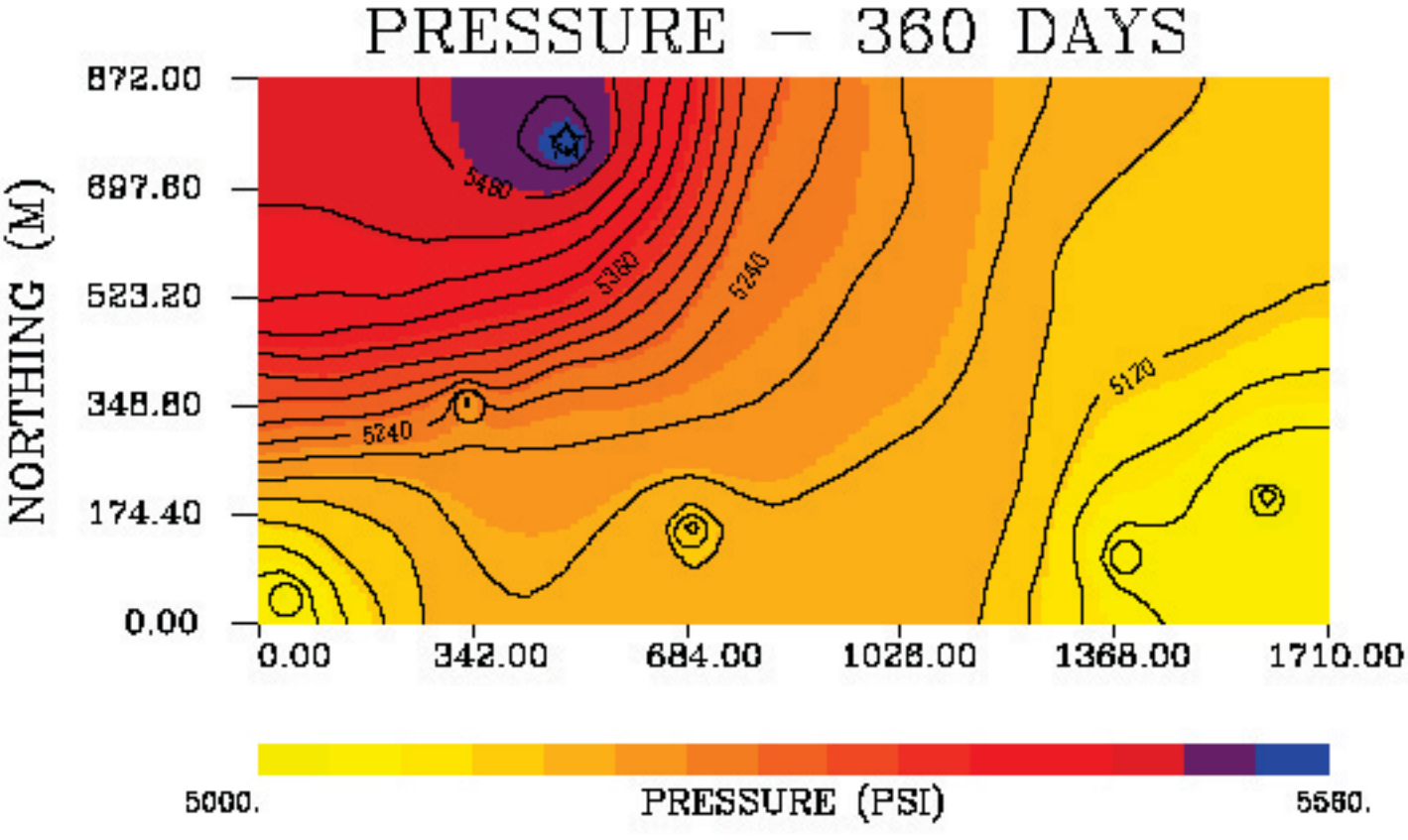
PRESSURE – 360 DAYS
872.00
697.60
523.20
348.80
174.40
0.00
NORTHING (M)
5460
5360
5240
5240
5120
0.00
342.00
684.00
1026.00
1368.00
1710.00
5000.
PRESSURE (PSI)
5560.

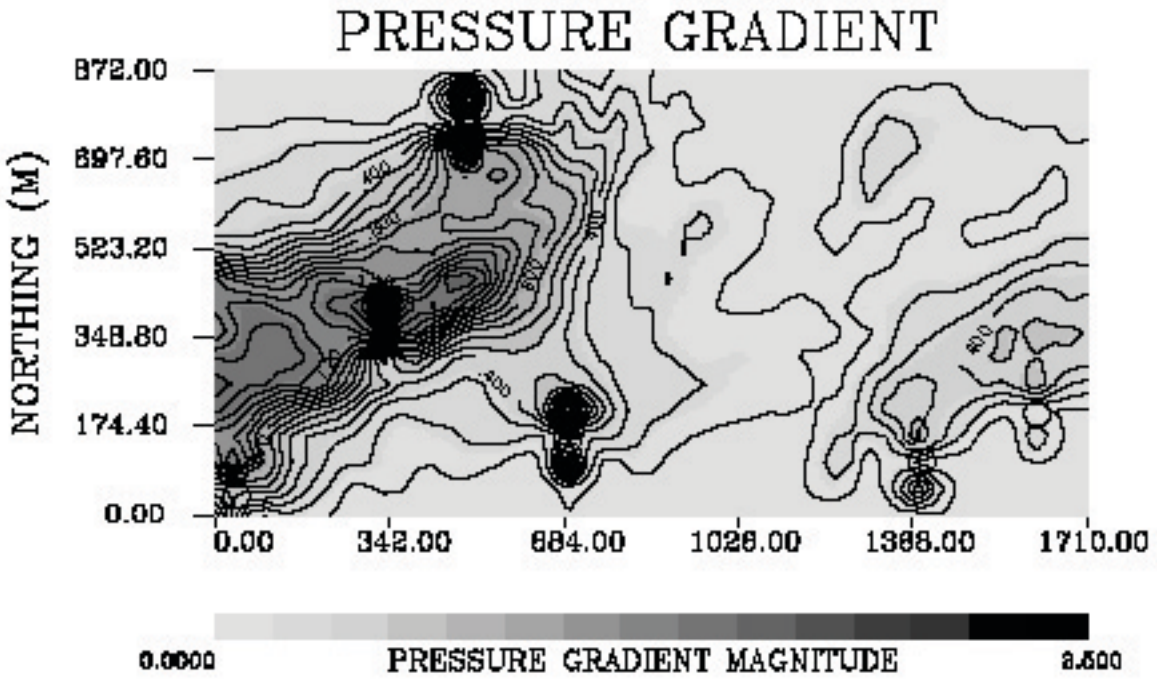
PRESSURE GRADIENT
872.00
697.60
523.20
348.80
174.40
0.00
NORTHING (M)
0.00
342.00
684.00
1026.00
1368.00
1710.00
0.0000
PRESSURE GRADIENT MAGNITUDE
0.500

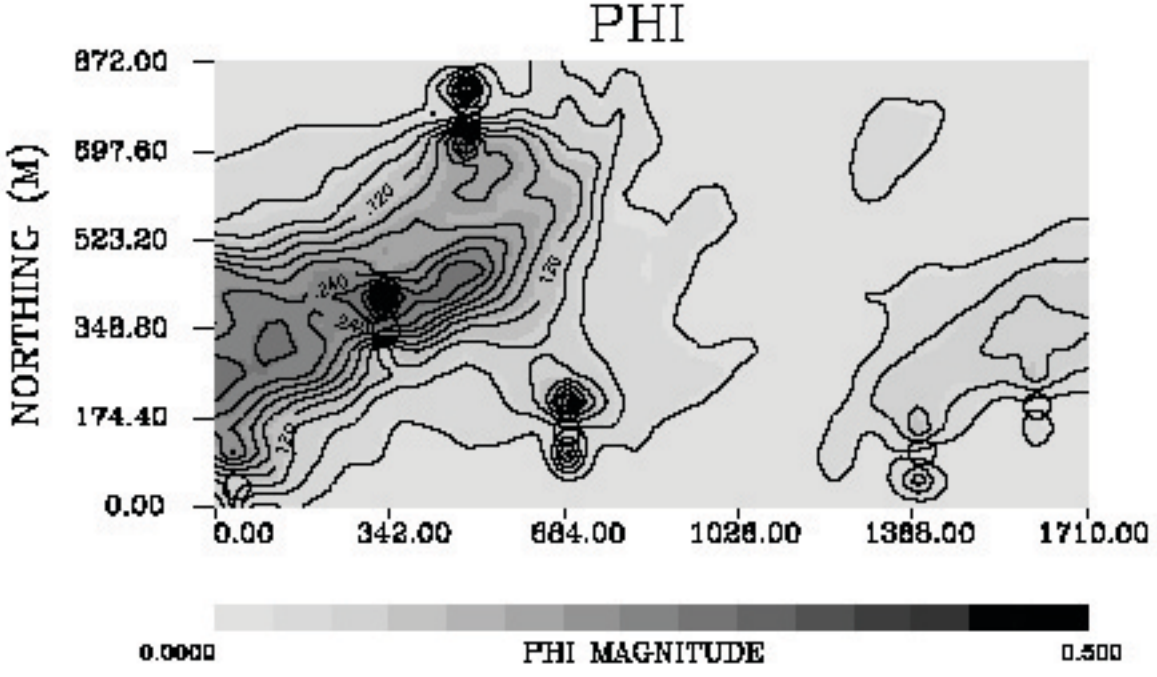
PHI
872.00
697.60
523.20
348.80
174.40
0.00
NORTHING (M)
0.00
342.00
684.00
1026.00
1368.00
1710.00
0.0000
PHI MAGNITUDE
0.500

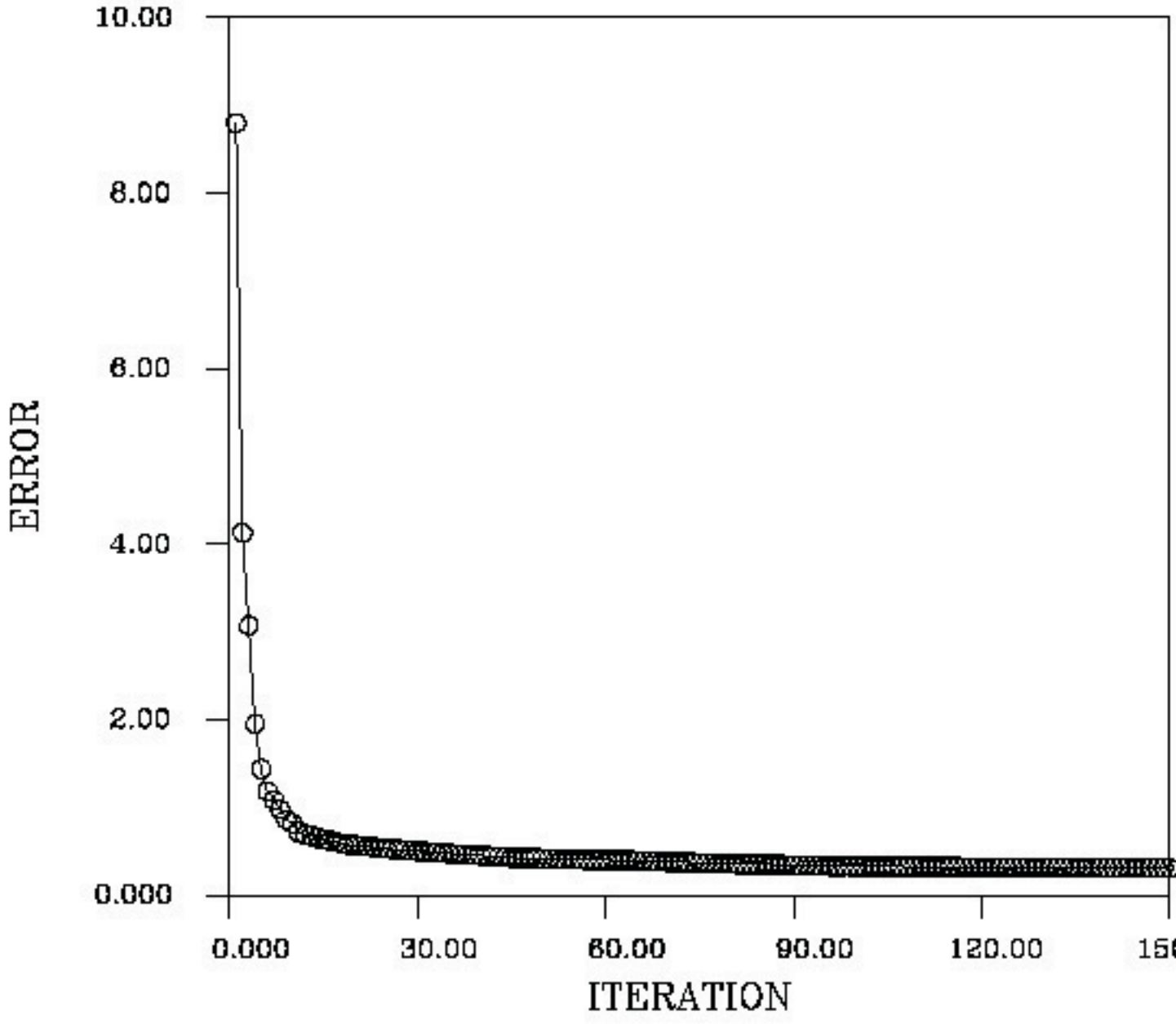
10.00
8.00
6.00
4.00
2.00
0.000
ERROR
0.000
30.00
60.00
90.00
120.00
ITERATION

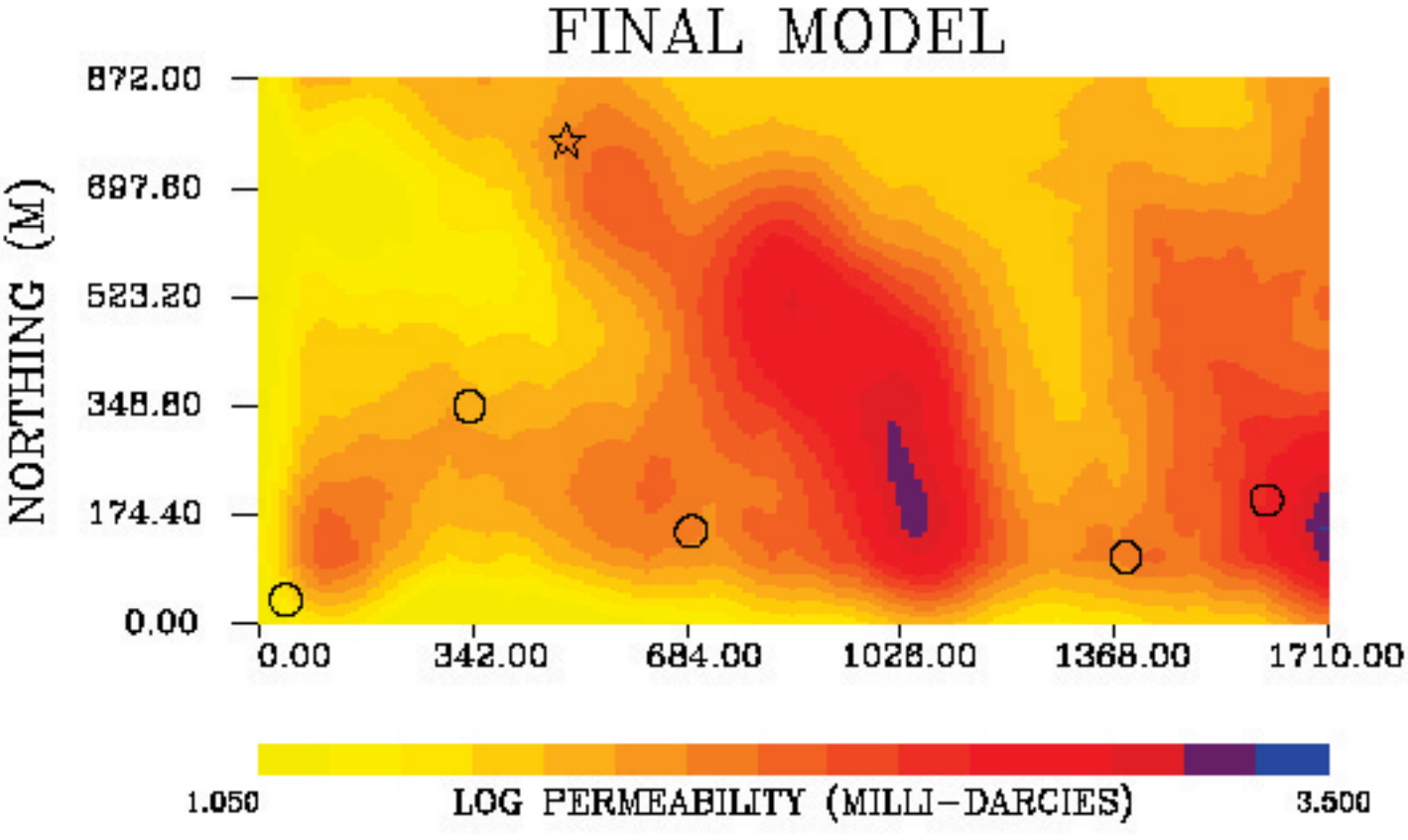
FINAL MODEL
872.00
697.60
523.20
348.80
174.40
0.00
NORTHING (M)
0.00
342.00
684.00
1026.00
1368.00
1710.00
1.050
LOG PERMEABILITY (MILLI-DARCIES)
3.500

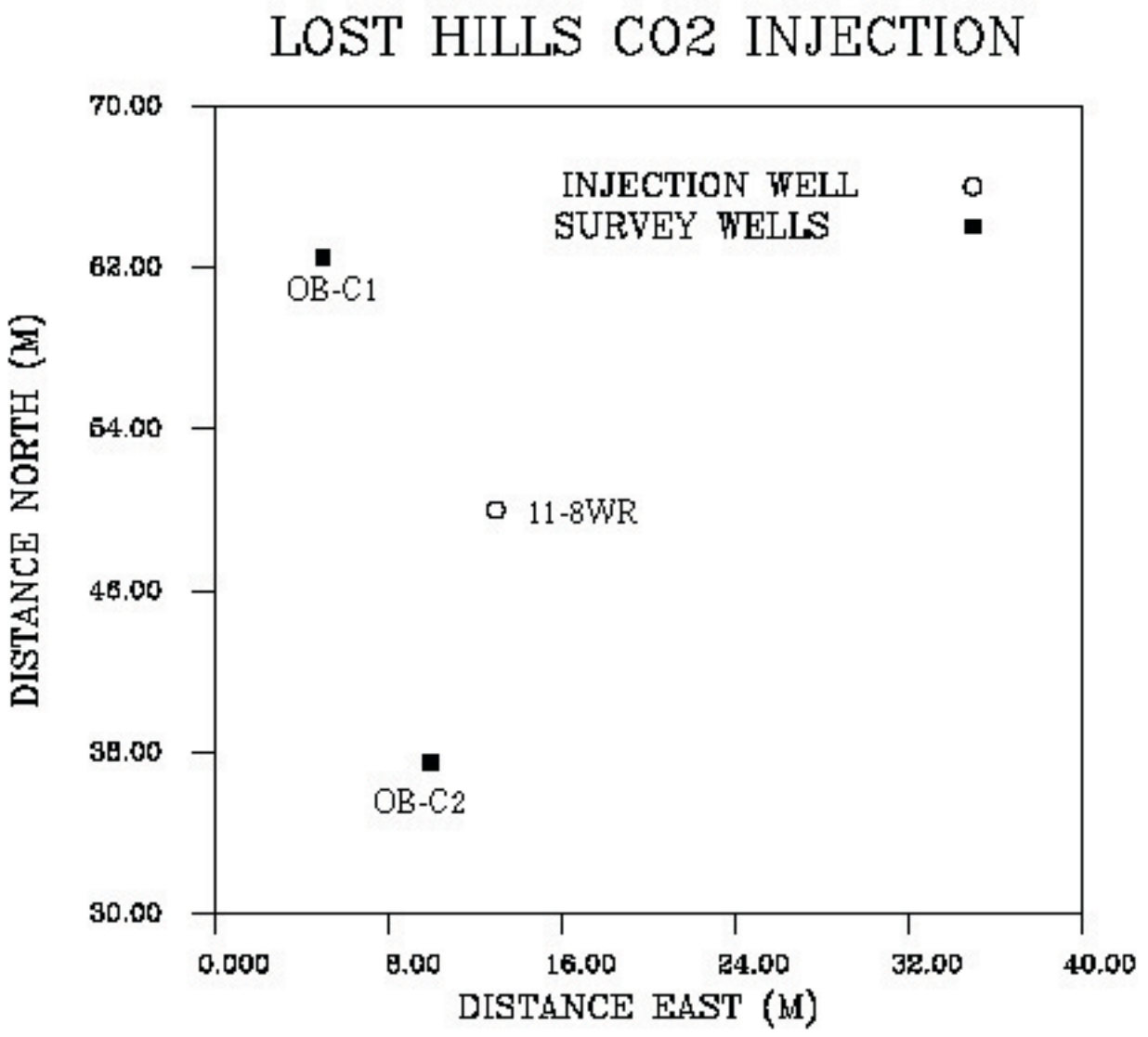
LOST HILLS CO2 INJECTION
INJECTION WELL
SURVEY WELLS
OB-C1
11-8WR
OB-C2
DISTANCE NORTH (M)
70.00
62.00
54.00
46.00
38.00
30.00
0.000
8.00
16.00
24.00
32.00
40.00
DISTANCE EAST (M)

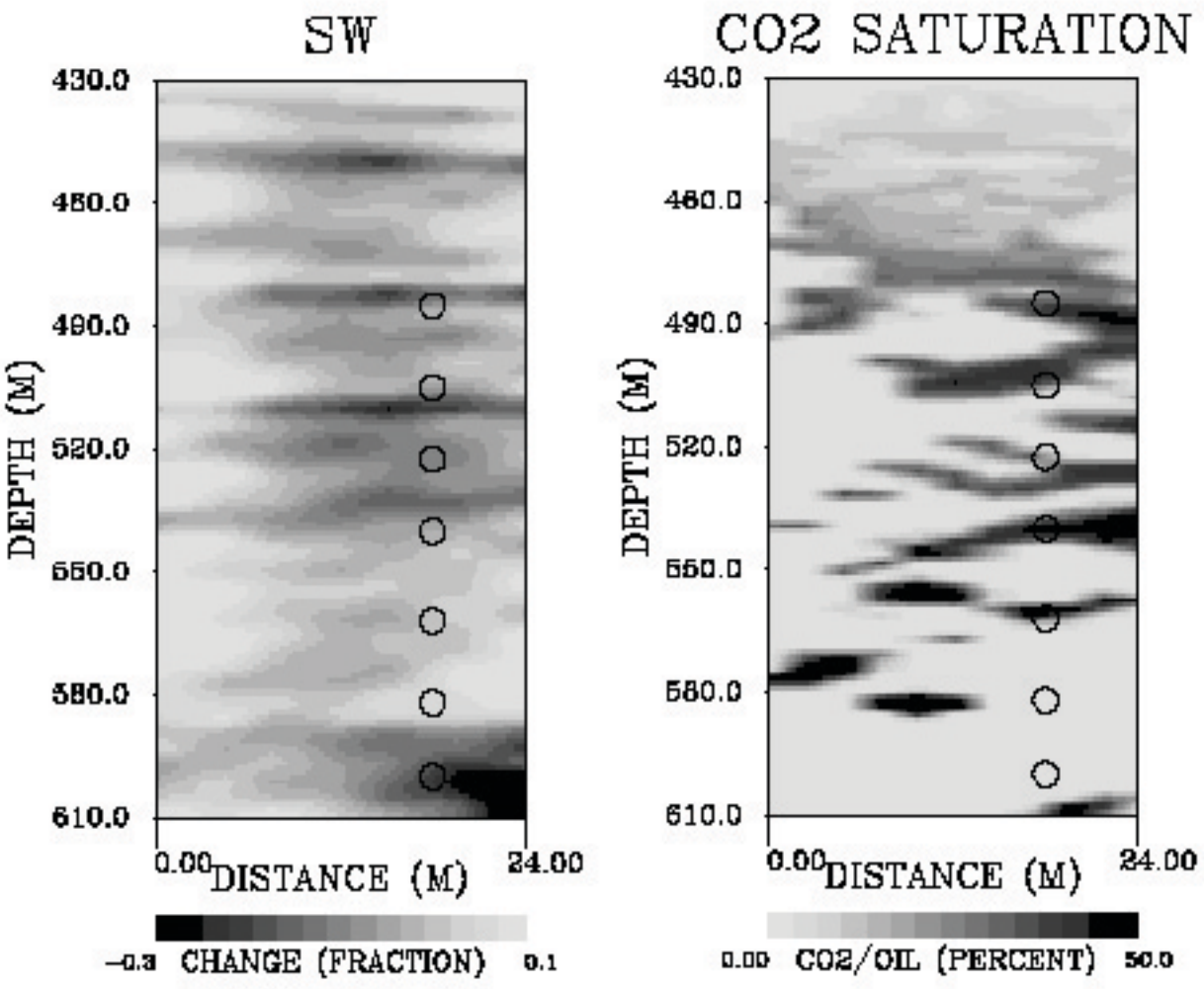
SW
CO2 SATURATION
430.0
460.0
490.0
520.0
550.0
580.0
610.0
DEPTH (M)
0.00
DISTANCE (M)
24.00
−0.3
CHANGE (FRACTION)
0.1
0.00
CO2/OIL (PERCENT)
50.0

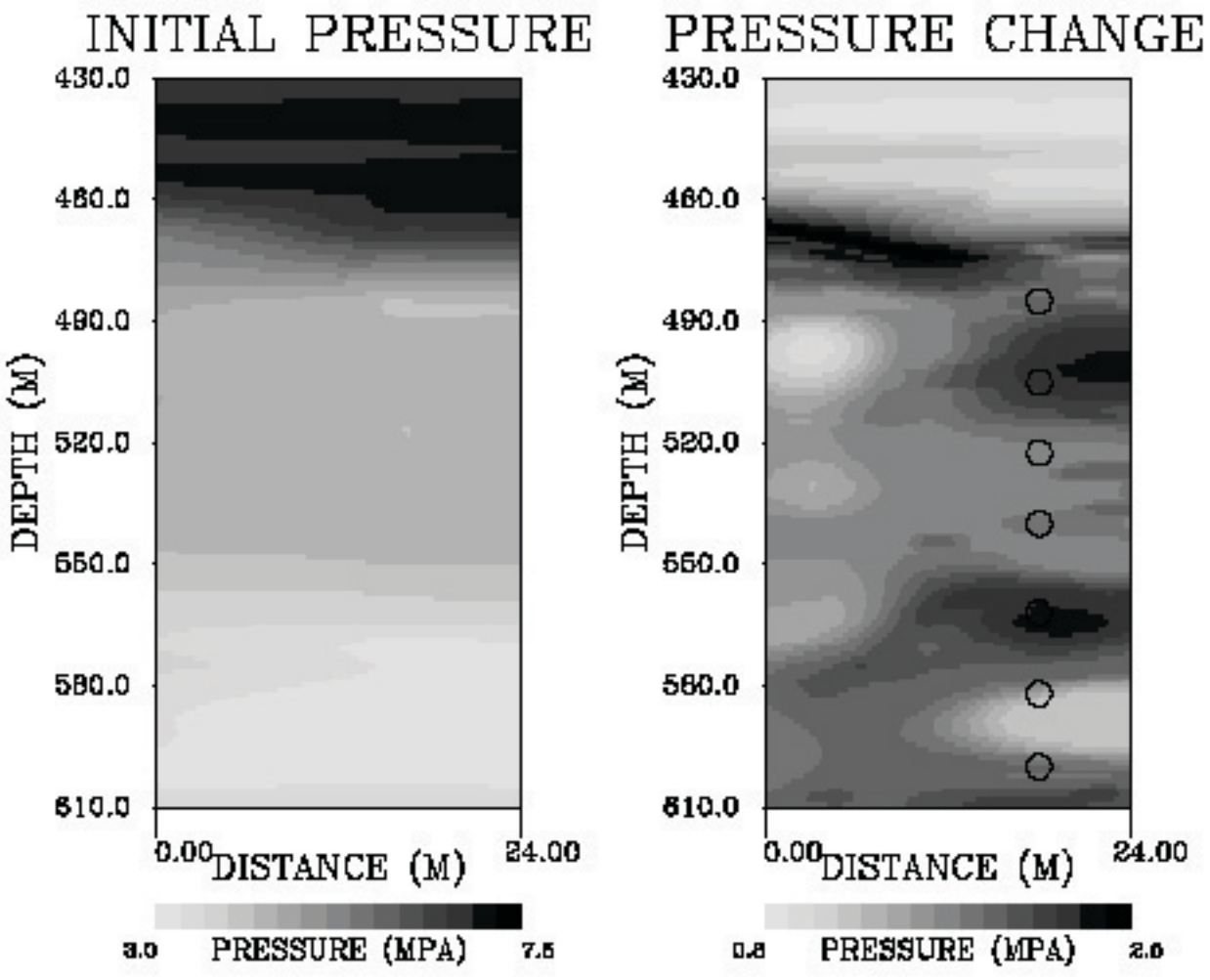
INITIAL PRESSURE
PRESSURE CHANGE
430.0
460.0
490.0
520.0
550.0
580.0
610.0
DEPTH (M)
0.00
DISTANCE (M)
24.00
3.0
PRESSURE (MPA)
7.5
0.8
2.6

# PERMEABILITY

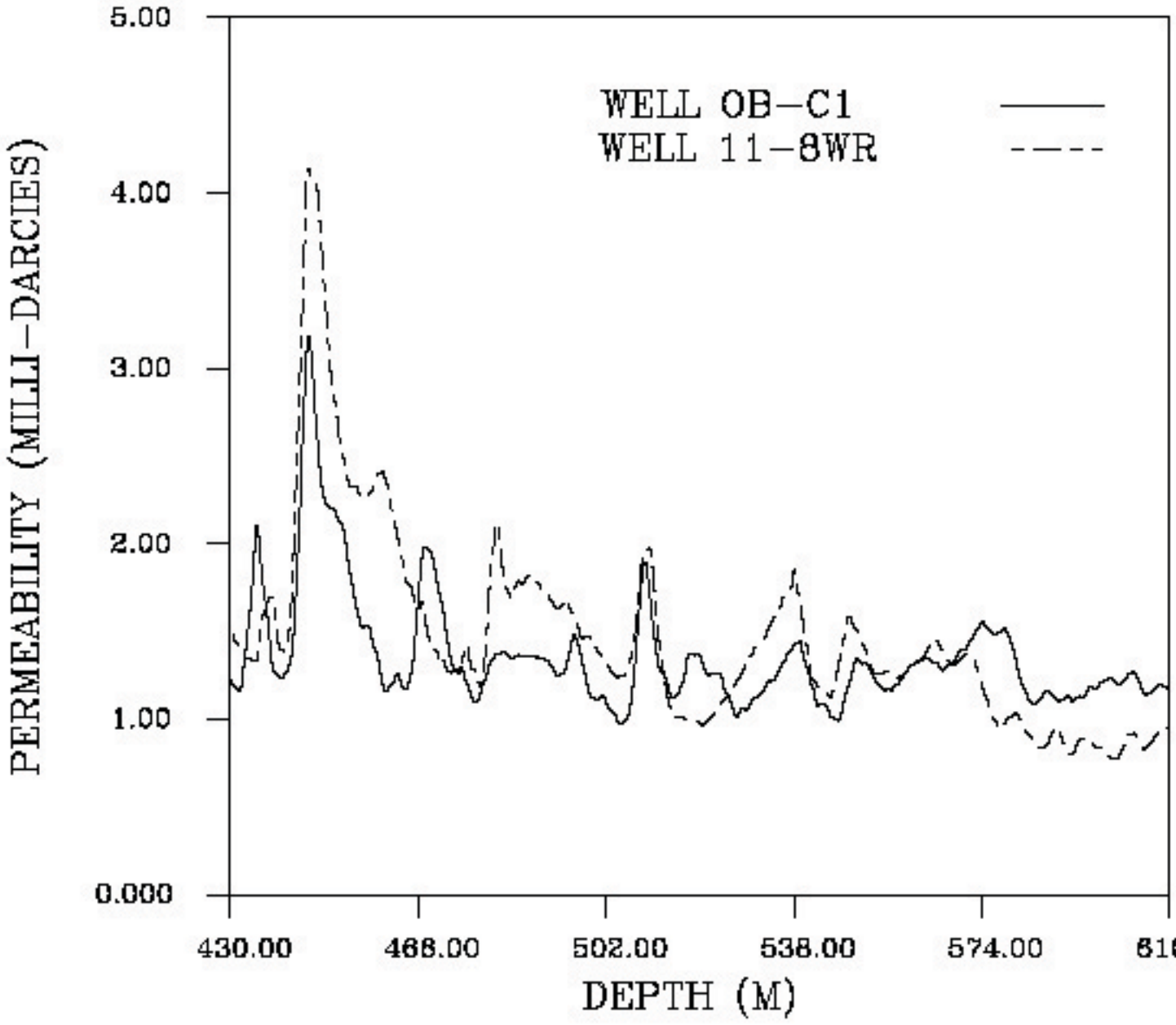

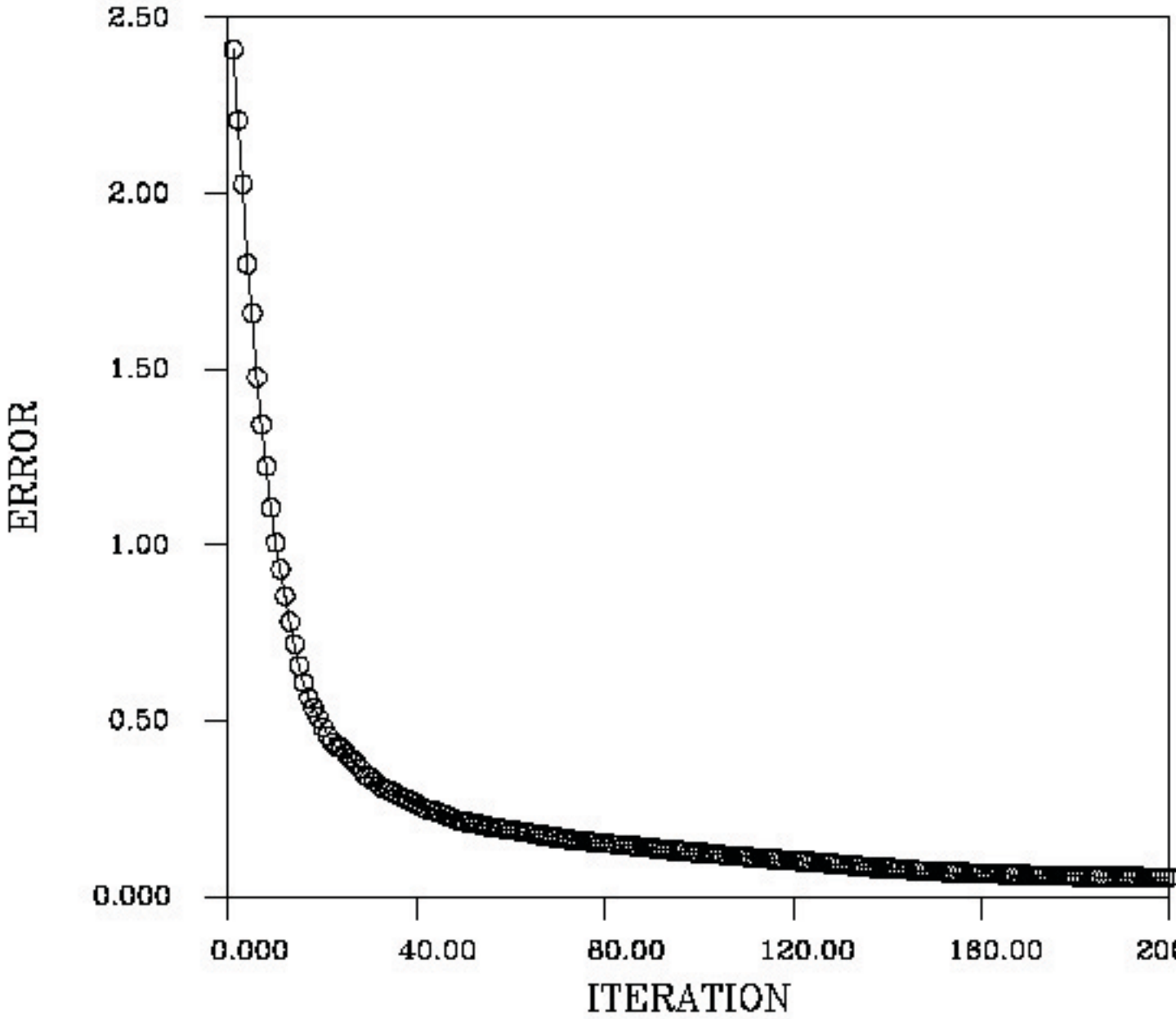
2.50
2.00
1.50
1.00
0.50
0.000
ERROR
0.000
40.00
80.00
120.00
160.00
200.
ITERATION

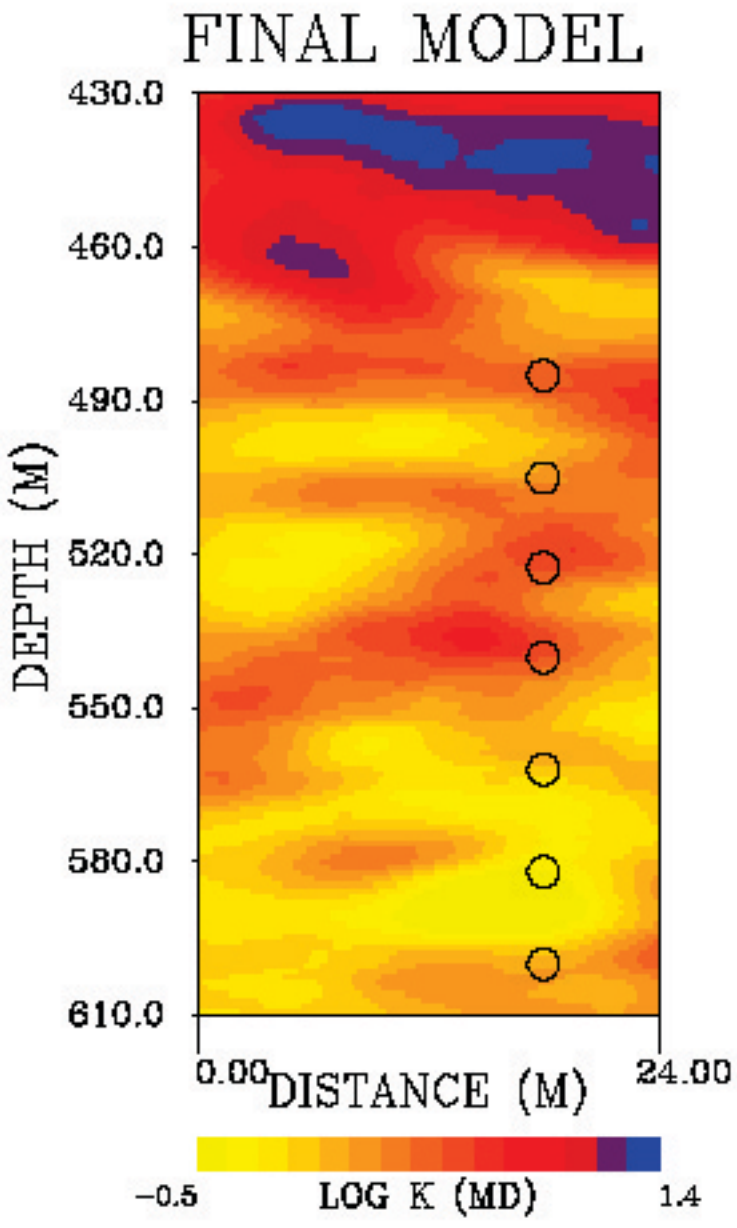
FINAL MODEL
430.0
460.0
490.0
520.0
550.0
580.0
610.0
DEPTH (M)
0.00
DISTANCE (M)
24.00
−0.5
LOG K (MD)
1.4

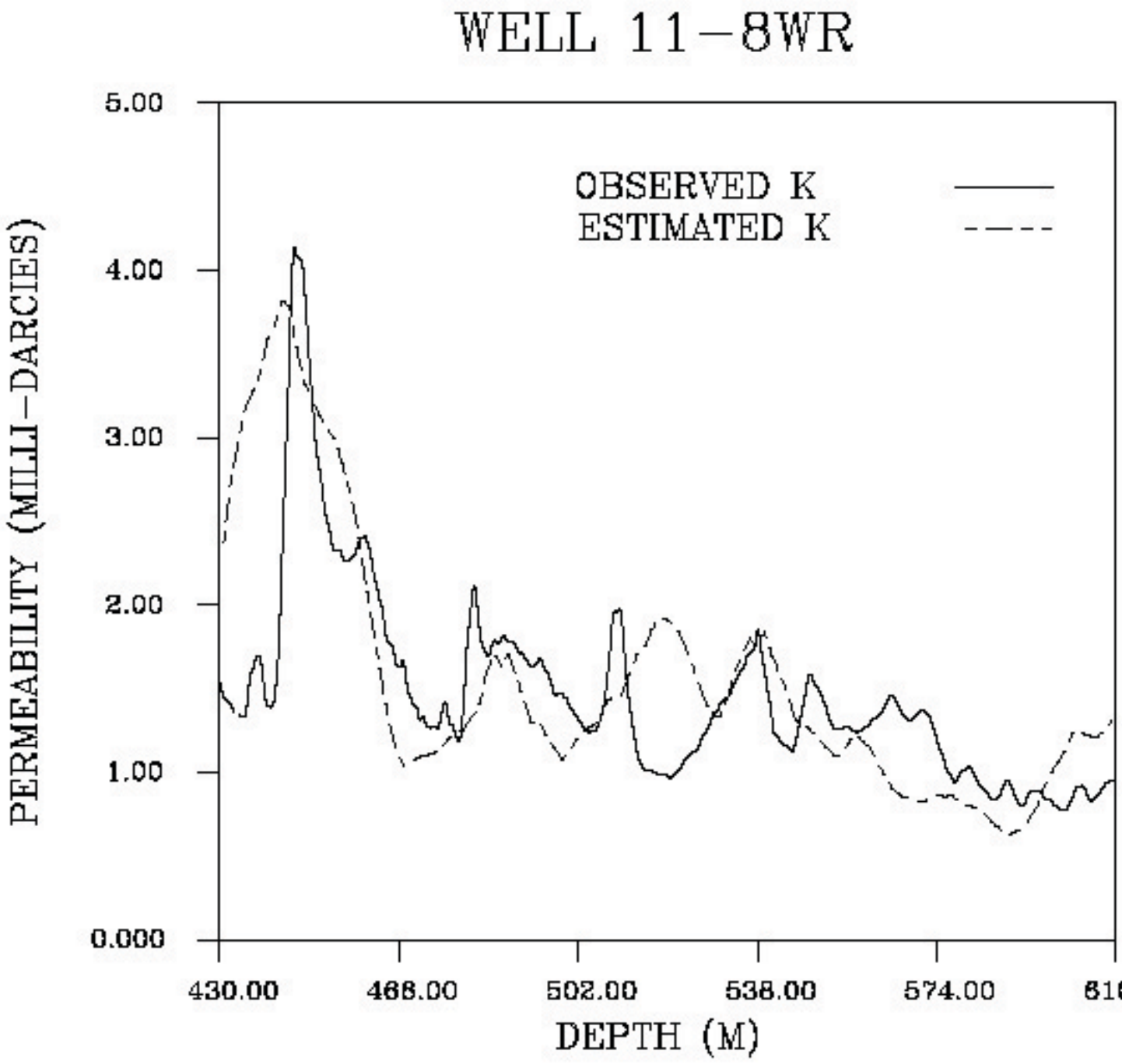
WELL 11-8WR
OBSERVED K
ESTIMATED K
PERMEABILITY (MILLI-DARCIES)
5.00
4.00
3.00
2.00
1.00
0.000
430.00
466.00
502.00
538.00
574.00
DEPTH (M)